

CRB-Guided Framework Design and Resource Allocation for Indoor mmWave ISCC Systems

Zhonghao Liu*, Yahao Ding*, Yinchao Yang*, and Mohammad Shikh-Bahaei*

*King's College London

Email: {zhonghao.liu, yahao.ding, yinchao.yang, m.sbahaei}@kcl.ac.uk

Abstract—Integrated sensing, communication, and computation (ISCC) provides a promising framework for indoor human-centric applications. In these applications, short-term human pose prediction facilitates continuous human tracking and resource allocation in advance. In this paper, we propose a Cramér–Rao bound (CRB) guided resource allocation framework for indoor mmWave ISCC systems to minimize the human pose prediction error under communication, latency, and energy constraints. We characterize the impact of sensing power on range-estimation uncertainty and point-cloud perturbation based on the CRB. To capture the impact of computation resources on prediction performance, we adopt an adaptive-depth Mamba-based pose prediction model, where lightweight prediction heads are attached after every layer to enable inference with different model depths. With this unified sensing-computation modeling, we establish a quantitative relationship among sensing power, model depth, and prediction error. Furthermore, we formulate a joint resource allocation problem to minimize the pose prediction error. To solve this problem efficiently, we develop an alternating optimization (AO)-based algorithm, where closed-form solutions are derived for the sensing power and model depth update steps. Simulation results show that the proposed scheme significantly reduces pose prediction error compared with baseline methods, validating its effectiveness for resource-constrained indoor human-centric ISCC systems.

Index Terms—ISCC, pose prediction, mmWave, resource allocation.

I. Introduction

Integrated sensing, communication, and computation (ISCC) has been regarded as a promising framework for next-generation intelligent wireless networks, since it enables wireless systems to improve resource efficiency by sharing spectrum and hardware resources [1]. With the development of intelligent wireless networks in indoor environments, sensing tasks are gradually evolving from conventional localization and detection toward human-centric applications, such as human motion monitoring and activity recognition [2]. Short-term human pose prediction plays an important role in such human-centric applications [3]. Specifically, the predicted positions of human joints can provide a prior estimate of the spatial structure and location of the human body. With this prior information, the access point (AP) can narrow the beam scanning region, select candidate sensing beams, and allocate resources in advance. In this context, millimeter-wave (mmWave) sensing has attracted increasing attention for indoor human-centric sensing tasks, as it can provide

privacy-preserving spatial observations from reflected radio signals [4].

Existing studies on ISAC/ISCC resource allocation have mainly focused on physical-layer performance from the perspective of wireless resource optimization. In [5], Liu et al. considered a RIS-assisted ISAC system with self-interference and maximized the communication sum rate under signal to noise ratio (SNR) and Cramér–Rao bound (CRB) constraints. In [6], Zhang et al. jointly optimized the beamforming matrix and power to maximize communication sum rate while satisfying CRB constraints. Ren et al. investigated the CRB-rate tradeoff in multi-antenna multicast ISAC channels by optimizing the transmit covariance matrix [7]. For indoor human sensing, mmWave radar has also been widely explored. Specifically, mmHPE was proposed in [8] to improve mmWave point-cloud quality through target boundary enhancement and perform multi-scale human pose estimation. Tang et al. proposed GF-DecNet in [9], which combines geometry-aware feature extraction with biomechanical constraints for robust human pose estimation.

However, physical-layer metrics cannot directly reflect the final performance of human sensing tasks. Moreover, existing learning-based mmWave human sensing methods usually focus on network architecture design under fixed sensing configurations. When the sensing power is reduced due to the competition from communication and computation, the received echo SNR decreases, leading to larger range-estimation uncertainty, which is further manifested as point-cloud jitter [10]. This perturbation can degrade pose prediction accuracy. Therefore, a quantitative link between physical-layer sensing quality and task-level performance is still lacking.

Beyond sensing uncertainty, the prediction performance is also affected by the computation resources. A deeper spatio-temporal network usually improves prediction performance [11], but increases computation energy and inference latency [12]. Under strict energy or delay constraints with a fixed computation frequency, full-layer inference may not be feasible. Therefore, the inference depth can be treated as a controllable computation resource to characterize the tradeoff between prediction accuracy and computation cost. Motivated by the above limitations, we consider an indoor mmWave ISCC framework that combines CRB-guided sensing uncertainty modeling with

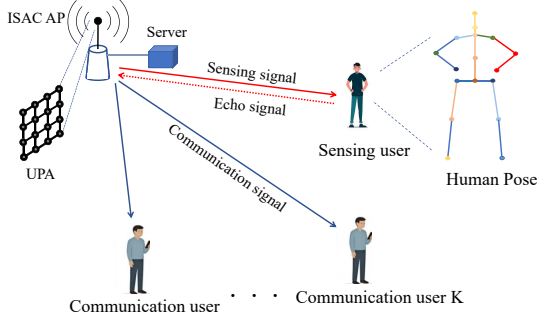


Fig. 1. Illustration of the considered indoor mmWave ISCC system for human pose prediction and tracking.

adaptive-depth pose prediction. The main contributions of this paper are summarized as follows:

- We establish a quantitative relationship among sensing power, model depth, and pose prediction error.
- We develop an adaptive-depth Mamba-based pose prediction model to enable flexible inference under energy and latency constraints.
- We formulate a joint resource allocation problem to minimize pose prediction error, and develop an AO-based algorithm with closed-form updates for efficient optimization.

II. System Model

As shown in Fig. 1, we consider an indoor mmWave ISCC system under limited resources where an AP equipped with a uniform planar array (UPA) consisting of $N_t = N_x N_z$ antenna elements serves K communication users and performs human sensing simultaneously. Frequency division is adopted to avoid interference between communication and sensing. At time slot t , the transmitted signal can be represented as:

$$\mathbf{x}[t] = \sum_{k=1}^K \sqrt{p_k} \mathbf{w}_{c,k} \mathbf{s}_{c,k}[t] + \sqrt{p_r} \mathbf{w}_r \mathbf{s}_r[t], \quad (1)$$

where p_k and p_r denote the communication power of user k and the sensing power, respectively. $\mathbf{s}_{c,k}[t]$ denotes the communication symbol for user k at time slot t , satisfying $\mathbb{E}[\mathbf{s}_{c,k}[t] \mathbf{s}_{c,k}^H[t]] = 1$. Similarly, $\mathbf{s}_r[t]$ denotes the sensing waveform satisfying $\mathbb{E}[\|\mathbf{s}_r[t]\|^2] = 1$. Communication and sensing signals are statistically independent, satisfying $\mathbb{E}[\mathbf{s}_{c,k}[t] \mathbf{s}_r^*[t]] = \mathbf{0}$, $\forall k$. $\mathbf{w}_{c,k} \in \mathbb{C}^{N_t}$ and $\mathbf{w}_r \in \mathbb{C}^{N_t}$ denote the communication beamforming vector for user k and the sensing beamforming vector, respectively. Specifically, \mathbf{w}_r is selected from a predefined unit-norm beam codebook $\mathcal{B} = \{\mathbf{a}(\theta_i, \phi_j)\}$, where (θ_i, ϕ_j) denotes a candidate azimuth-elevation direction. For the considered UPA employed in the Oxz plane, $\mathbf{a}(\theta_i, \phi_j)$ is given by: $\mathbf{a}(\theta_i, \phi_j) = \mathbf{a}_x(\theta_i, \phi_j) \otimes \mathbf{a}_z(\theta_i, \phi_j)$, where the horizontal steering vector $\mathbf{a}_x(\theta_i, \phi_j)$ can be given by $\left[1, e^{j \frac{2\pi d}{\lambda} \sin(\phi_j) \cos(\theta_i)}, \dots, e^{j(N_x-1) \frac{2\pi d}{\lambda} \sin(\phi_j) \cos(\theta_i)}\right]^T$, and

the vertical steering vector $\mathbf{a}_z(\theta_i, \phi_j)$ is denoted by $\left[1, e^{j \frac{2\pi d}{\lambda} \sin(\phi_j)}, \dots, e^{j(N_z-1) \frac{2\pi d}{\lambda} \sin(\phi_j)}\right]^T$.

The communication beamforming vector is designed using zero-forcing (ZF) precoding to suppress inter-user interference. Thus, the received signal of communication user k at time slot t can be written as:

$$y_k[t] = \sqrt{p_k} \mathbf{h}_k^H \mathbf{w}_{c,k} \mathbf{s}_{c,k}[t] + n, \quad (2)$$

where $\mathbf{h}_k \in \mathbb{C}^{N_t}$ denotes the downlink channel between the AP and user k , and $n \sim \mathcal{CN}(0, \sigma_n^2)$ is the additive white Gaussian noise. For notational simplicity, the time index is omitted in the following. Based on the predicted positions of human joints from the previous time slot, the AP selects P candidate beams from the codebook and scans them sequentially within the current time slot. Thus, at time slot t , the echo signal can be given by:

$$\mathbf{e}[t] = \sum_{p=1}^P \beta_p \sqrt{p_r} \mathbf{A}_p \mathbf{w}_{r,p} \mathbf{s}_r \left(t - \frac{2d_p}{c}\right) + z, \quad (3)$$

where $\beta_p = \zeta/2d_p$ is the path-loss coefficient, d_p is the propagation distance, ζ is the radar cross section (RCS), $\mathbf{A}_p = \mathbf{a}(\theta_p, \phi_p) \mathbf{a}^H(\theta_p, \phi_p)$ denotes the directional response matrix associated with the p -th scanned beam, $\mathbf{w}_{r,p}$ is the p -th scanned sensing beam at time slot t , c is the speed of light, and $z \sim \mathcal{CN}(0, \sigma_z^2)$ is the additive white Gaussian noise.

Following (2), the communication SNR of user k is:

$$\text{SNR}_k = \frac{p_k |\mathbf{h}_k^H \mathbf{w}_{c,k}|^2}{\sigma_n^2}. \quad (4)$$

Following (3), the echo SNR corresponding to the p -th scanned beam can be denoted as:

$$\text{SNR}_p = \frac{\zeta^2 p_r}{4d_p^4 \sigma_z^2}. \quad (5)$$

Following [10], the uncertainty in the estimated distance can be characterized by the CRB, which can be denoted by:

$$\sigma_{d,p}^2 = \frac{c^2}{8\pi^2 \text{SNR}_p B_r^2}, \quad (6)$$

where B_r is the bandwidth of sensing. Based on that, the estimated distance \tilde{d}_p can be denoted by $\tilde{d}_p = d_p + \Delta d_p$, where $\Delta d_p \sim \mathcal{N}(0, \sigma_{d,p}^2)$. The estimated distance set $\tilde{\mathbf{D}} = \{\tilde{d}_p\}$ can be further mapped into point clouds, where the point corresponding to the p -th beam is represented by $\mathbf{P}_p = \tilde{d}_p [\cos \theta_p \cos \phi_p, \cos \theta_p \sin \phi_p, \sin \theta_p]^T$.

III. ADAPTIVE-DEPTH MAMBA-BASED POSE PREDICTION

When sensing power is reduced due to resource competition with communication and computation, the resulting range-estimation uncertainty is manifested as point-cloud jitter. To improve pose prediction performance under this perturbation and resource constraints, we propose an

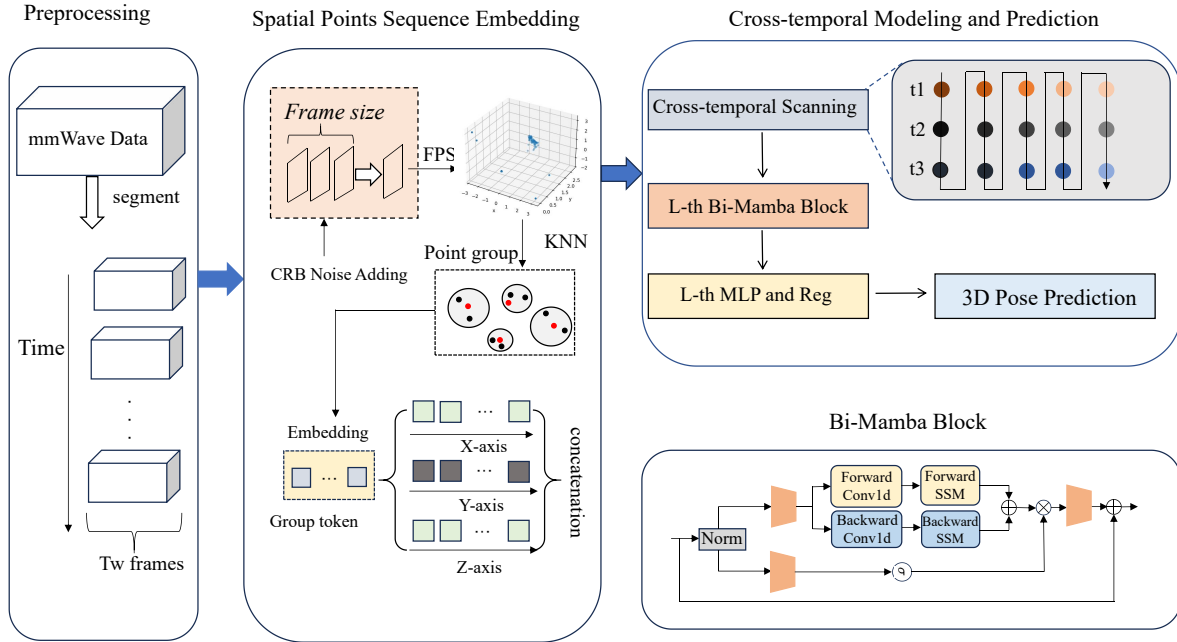


Fig. 2. Architecture of the proposed CRB-Mamba framework for mmWave point-cloud-based human pose prediction.

adaptive-depth CRB-Mamba framework, as shown in Fig. 2.

For point-cloud perturbation modeling, SNR_o is defined as the sensing SNR of the frame center point. SNR_p is obtained by scaling SNR_o according to its relative range, and the corresponding CRB-derived variance is calculated by (6). To model the temporal dependencies efficiently, we adopt a bidirectional Mamba (Bi-Mamba) network as the backbone because its selective state-space model enables efficient long-sequence modeling with linear complexity. The discrete state-space model can be written as

$$\mathbf{h}_b = \bar{\mathbf{A}}\mathbf{h}_{b-1} + \bar{\mathbf{B}}\mathbf{x}_b, \quad \mathbf{y}_b = \bar{\mathbf{C}}\mathbf{h}_b + \bar{\mathbf{D}}\mathbf{x}_b, \quad (7)$$

where $\mathbf{x}_b \in \mathbb{R}^d$, $\mathbf{h}_b \in \mathbb{R}^N$, and $\mathbf{y}_b \in \mathbb{R}^d$ denote the input, hidden state, and output at time step b , respectively. The matrices $\bar{\mathbf{A}}$, $\bar{\mathbf{B}}$, $\bar{\mathbf{C}}$, and $\bar{\mathbf{D}}$ are learnable parameters.

For each frame, we first select a set of representative group centers using farthest point sampling (FPS), and then construct local neighborhoods around each center via K -nearest neighbors (KNN). Each neighborhood is normalized by subtracting its center to obtain relative coordinates. After serializing the original point cloud into a 1D sequence, we employ a 6-layer Bi-Mamba network for training. Considering that edge-side power consumption and delay constraints may limit the execution of full network inference, we attach a lightweight prediction head after each Bi-Mamba layer, enabling the model to still output the corresponding pose prediction results when full-layer inference is infeasible. During training, the original action sequence is partitioned into overlapping samples by a sliding window of length T_w . Each clip is

used as one training sample, and the model predicts the 3D joint coordinates of the next frame. The network is optimized with Adam. Each frame contains J joints, and the predicted and ground-truth coordinates of joint j in the cp -th clip are denoted by $\hat{\mathbf{p}}_j^{(cp)}$ and $\mathbf{p}_j^{*(cp)}$, respectively.

$$\mathcal{L}_{\mathcal{MSE}} = \frac{1}{N_b J} \sum \sum \|\hat{\mathbf{p}}_j^{(cp)} - \mathbf{p}_j^{*(cp)}\|_2^2, \quad (8)$$

where N_b is the batch size.

IV. PROBLEM FORMULATION AND SOLUTION

A. Problem Formulation

The energy consumption of the AP consists of three parts: sensing transmission energy E_r , communication transmission energy E_c , and local computation energy E_{comp} . Let C_{pc} denote the CPU cycles required for point-cloud generation in one time slot, C_b represent the layer-independent CPU cycles required for feature construction and the final prediction head, and C_L denote the CPU cycles required by each inference layer. Thus, the computation latency and energy can be expressed as:

$$\tau_{\text{comp}} = \frac{C_{pc} + C_b + L C_L}{f}, \quad (9)$$

$$E_{\text{comp}} = \gamma(C_{pc} + C_b + L C_L) f^2, \quad (10)$$

where f is the fixed computation frequency. Let $m(p_r, L)$ denote the prediction error, the optimization problem is given by:

$$\min_{p_r, L, \{p_k\}_{k=1}^K} m(p_r, L) \quad (11a)$$

$$\text{s.t. } T_0 + \tau_{\text{comp}} \leq T, \quad (11b)$$

$$E_c + p_r T_0 + E_{\text{comp}} \leq P_{\text{max}} T, \quad (11c)$$

$$\text{SNR}_k \geq \text{SNR}_{\text{min}}, \quad \forall k, \quad (11d)$$

$$\text{SNR}_o \geq \gamma_{\text{min}}^{\text{det}}, \quad (11e)$$

$$1 \leq L \leq L_{\text{max}}, \quad L \in \mathbb{Z}_+, \quad (11f)$$

$$0 \leq p_r + \sum_{k=1}^K p_k \leq P_t, \quad (11g)$$

where T_0 denotes the sensing duration within one time slot, and P_{max} denotes the maximum allowable average power. SNR_{min} is the minimum communication SINR threshold, while $\gamma_{\text{min}}^{\text{det}}$ denotes the minimum sensing SNR required for target detectability. In addition, P_t is the maximum total transmit power at the AP. Constraint (11b) requires that the sensing duration and the computing latency should not exceed the total slot duration. Constraint (11c) represents the total energy budget. Constraint (11d) guarantees the communication QoS and (11e) ensures that the sensing SNR at the target center remains above a prescribed threshold. Constraints (11f) and (11g) specify the feasible domains of the optimization variables.

B. Problem Solution

Before optimizing the sensing power and the model depth, the communication power required to satisfy the QoS constraints of all users is first determined.

1) Empirical Modeling of Prediction Error: We use the mean per-joint position error (MPJPE) to evaluate the pose prediction performance. MPJPE measures the average Euclidean distance between the predicted 3D joint coordinates and the corresponding ground-truth joint coordinates over all joints and testing samples. A smaller MPJPE indicates more accurate pose prediction. After multiple runs and evaluations, we obtain the fitted curve shown in Fig. 3. The empirical results indicate that MPJPE decreases monotonically with both p_r and L . This is because a larger sensing power reduces jitter, while a larger inference depth improves the spatio-temporal representation capability of the pose prediction model.

2) Minimum Communication Power with Fixed Beam Directions: The minimum communication power required to support all users is obtained by solving

$$\min_{\{p_k\}} \sum_{k=1}^K p_k \quad (12a)$$

$$\text{s.t. } 0 \leq p_k \leq P_t, \quad \forall k, \quad (12b)$$

$$(11d)$$

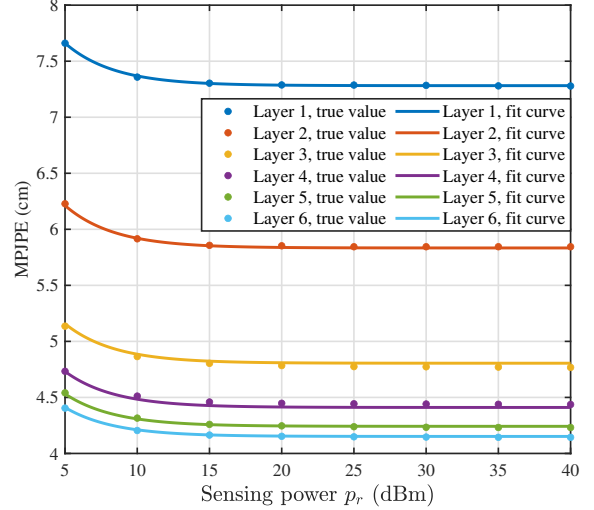


Fig. 3. Fitted MPJPE curves under different sensing power and model depth.

(12) can be efficiently solved using CVX. Let P_c^{min} denote its optimal value. Hence, once the minimum communication power is obtained, the problem (11) is reduced to the joint optimization of the model depth L and the sensing transmit power p_r , which can be expressed as:

$$\min_{p_r, L} m(p_r, L) \quad (13a)$$

$$p_r T_0 + E_{\text{comp}} \leq \tilde{E}_{\text{max}}, \quad (13b)$$

$$0 \leq p_r \leq \tilde{P}_t, \quad (13c)$$

$$(11b), (11e), (11f),$$

where \tilde{P}_t is $P_t - P_c^{\text{min}}$ and \tilde{E}_{max} is $P_{\text{max}} T - P_c^{\text{min}} T$.

3) AO-Based Algorithm: To solve problem (13a), we adopt an alternating optimization (AO)-based algorithm. Since the fitted error function $m(p_r, L)$ decreases monotonically with both p_r and L , the original problem can be decomposed into two subproblems and solved alternately.

We first apply a continuous relaxation by relaxing the integer constraint $L \in \mathbb{Z}_+$ to the interval $L \in [1, L_{\text{max}}]$. For a given sensing transmit power p_r , the subproblem 1 with respect to the model depth L is formulated as

$$\min_L m(L) \quad (14)$$

$$\text{s.t. } (11b), (11f), (13b)$$

According to the latency constraint (11b), we have the following upper bound on the model depth:

$$L_\tau = \frac{f(T - T_0) - C_{pc} - C_b}{C_L}. \quad (15)$$

According to the energy constraint (13b), we have another upper bound on the model depth:

$$L_E = \frac{\tilde{E}_{max} - p_r T_0 - \gamma(C_{pc} + C_b)f^2}{\gamma C_L f^2}. \quad (16)$$

By combining (15), (16), and the feasible range of L , the optimal solution to the relaxed problem can be expressed in closed form as

$$L^* = \max \{1, \lfloor \min \{L_{max}, L_\tau, L_E\} \rfloor\}, \quad (17)$$

where $\lfloor \cdot \rfloor$ denotes the floor operation, which returns the largest integer no greater than its argument.

Similarly, for a given model depth L , the subproblem 2 with respect to the transmit power p_r is formulated as

$$\begin{aligned} \min_{p_r} \quad & m(p_r) \\ \text{s.t.} \quad & (11e), (13b), (13c). \end{aligned} \quad (18)$$

According to the constraint (13b), we have an upper bound on the sensing transmit power:

$$P_E = \frac{\tilde{E}_{max} - E_{comp}}{T_0}. \quad (19)$$

In addition, according to the sensing detectability constraint (11e), the sensing power should also satisfy the following lower bound:

$$P_r^{\min} = \frac{4d_p^4 \sigma_z^2 \gamma_{\min}^{\det}}{\zeta^2}. \quad (20)$$

By combining (19), (20), and the feasible range of p_r , the optimal sensing power can be expressed in closed form as

$$p_r^* = \min \{ \tilde{P}_t, P_E \}, \quad \text{subject to } p_r^* \geq P_r^{\min}. \quad (21)$$

With the closed-form updates of L and p_r , the proposed method can be implemented through an AO-based iterative procedure, as summarized in Algorithm 1. The minimum communication power is computed only once, while both the depth update and the sensing power update have closed-form solutions. Therefore, if the AO procedure converges in I iterations, the overall complexity is $O(K^3 + I)$.

V. Simulation And Results Analysis

We conduct numerical simulations to evaluate the proposed model. The simulation parameters are summarized in Table I. The hidden feature dimension of the Bi-Mamba network is set to 384, and the window length is set to $T_w = 8$. To evaluate the effectiveness of joint sensing-computation optimization, two baseline schemes are considered. The fixed $L = 1$ baseline minimizes computation cost and allocates more resources to improve sensing quality, while the fixed $p_r = P_r^{\min}$ baseline only satisfies the minimum sensing detectability requirement and uses the remaining resources to select the largest feasible inference depth. Fig. 4 shows the MPJPE performance versus the CPU frequency f . As f increases,

Algorithm 1 AO-Based Joint Optimization Algorithm

Require: System parameters, I_{max} , and convergence tolerance ϵ .

Ensure: Optimized communication power $\{p_k^*\}_{k=1}^K$, sensing power p_r^* , and model depth L^* .

- 1: Initialize $i = 0$, $L^{(0)} = 1$, and $p_r^{(0)} = P_r^{\min}$, where P_r^{\min} is obtained by (20).
 - 2: Obtain the minimum communication power P_c^{\min} by solving problem (12).
 - 3: Update \tilde{P}_t and \tilde{E}_{max} .
 - 4: repeat
 - 5: Obtain L^{i+1} by (17).
 - 6: Obtain $p_r^{(i+1)}$ by (21).
 - 7: Set $i = i + 1$.
 - 8: until the convergence criterion is satisfied
 - 9: return $\{p_k^*\}_{k=1}^K$, $p_r^* = p_r^{(i)}$, and $L^* = L^{(i)}$.
-

TABLE I
Simulation Parameters

Parameter	Value
Number of terminals, K	4
UPA size, (N_x, N_z)	(4, 4)
Noise power, σ_n^2, σ_z^2	10^{-6}
Sensing bandwidth B_r	0.5 GHz
Minimum communication SNR, SNR_{\min}	5
Slot duration, T	0.1 s
Transmission duration, T_0	0.05 s
Minimum sensing SNR threshold, γ_{\min}^{\det}	-5dB
Computation frequency, f	100 MHz
Maximum Bi-Mamba depth, L_{max}	6
Effective switched-capacitance coefficient, γ	10^{-25}
CPU cycles for point-cloud generation, C_{pc}	128*256*8
Layer-independent CPU cycles, C_b	384*96*8
CPU cycles per Bi-Mamba layer, C_L	384*96*8*4

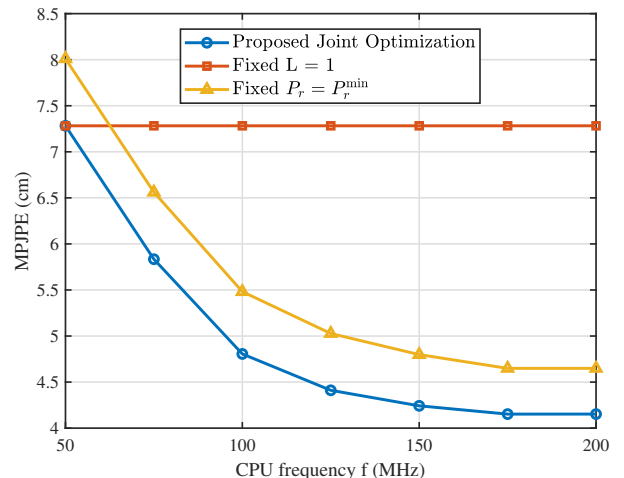


Fig. 4. MPJPE versus CPU frequency.

the proposed method significantly reduces the MPJPE, especially in the low-frequency region, because a higher

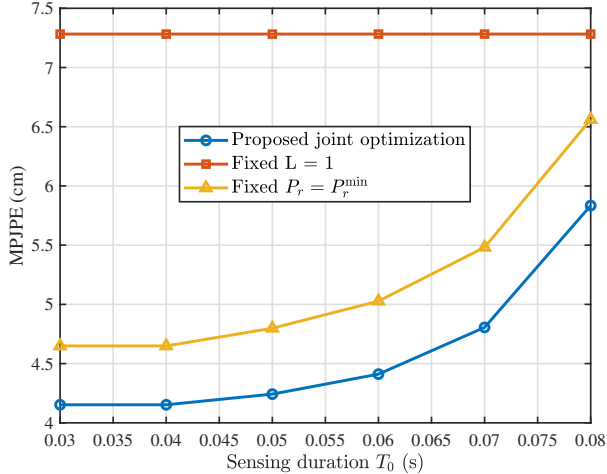


Fig. 5. MPJPE versus sensing duration T_0 .

CPU frequency relaxes the latency constraint and enables a deeper inference model. When f exceeds around 150 MHz, the performance gradually saturates, since the model depth approaches its upper limit. Compared with the fixed $L = 1$ baseline, the proposed method reduces the MPJPE by about 43% in the high-frequency region. Compared with the fixed $p_r = P_r^{\min}$ baseline, it achieves about 10%–13% improvement, showing the benefit of jointly optimizing sensing power and model depth.

Fig. 5 presents the MPJPE performance under different sensing durations T_0 . The proposed method maintains a low MPJPE when T_0 is moderate, while the error increases when T_0 becomes large. This is because a larger T_0 reduces the available computation time $T - T_0$ and tightens the energy budget. Compared with the fixed $L = 1$ baseline, the proposed method achieves about 43% MPJPE reduction when T_0 is moderate and still maintains about 20% improvement when $T_0 = 0.08$ s. Compared with the fixed $p_r = P_r^{\min}$ baseline, it consistently achieves about 10%–12% improvement.

Fig. 6 illustrates the impact of the maximum allowable average power on MPJPE. When the power budget is limited, all schemes suffer from high prediction error due to insufficient sensing and computation resources. As the power budget increases from 26 dBm to 27 dBm, the proposed method sharply reduces the MPJPE from above 7 cm to about 4.4 cm, and then gradually saturates after around 28 dBm. Compared with the fixed $L = 1$ baseline, the proposed method reduces the MPJPE by about 42% in the medium-to-high power region. Compared with the fixed $p_r = P_r^{\min}$ baseline, it achieves about 10%–12% improvement, confirming the effectiveness of joint sensing-computation resource allocation.

VI. Conclusion

In this paper, we proposed a human-centric sensing framework for indoor mmWave ISCC systems. The pro-

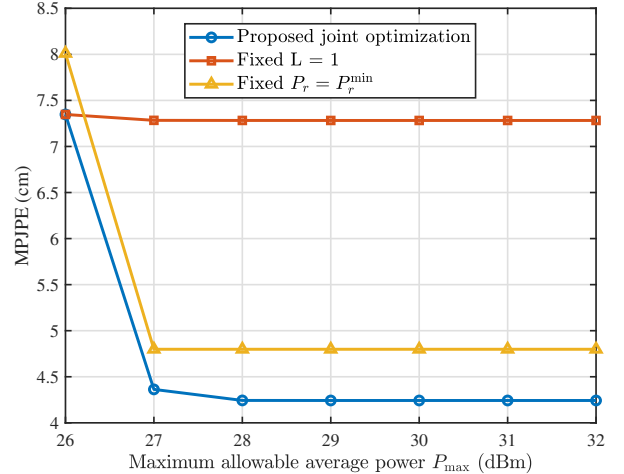


Fig. 6. MPJPE versus maximum allowable average power P_{max} .

posed framework jointly considers CRB-guided sensing uncertainty and model-depth selection to improve human pose prediction performance under limited resources. We established a quantitative relationship among sensing power, model depth, and pose prediction error. Based on the relationship, we formulated a joint resource allocation problem to minimize the pose prediction error. To solve this problem, we developed an AO-based joint optimization algorithm, where closed-form update rules were derived for efficient optimization. Simulation results demonstrate that the proposed method effectively reduces pose prediction error compared with baseline schemes. Future work will extend the framework to multiple sensing users in diverse indoor scenarios with more complex human motion patterns.

References

- [1] D. Wen, Y. Zhou, X. Li, Y. Shi, K. Huang, and K. B. Letaief, "A survey on integrated sensing, communication, and computation," *IEEE Communications Surveys & Tutorials*, vol. 27, no. 5, pp. 3058–3098, 2025.
- [2] W. Chen, Y. He, G. Yu, J. Wang, and H. Luo, "Sensing framework design and performance optimization with action detection for iscc," *IEEE Transactions on Wireless Communications*, 2025.
- [3] T. Fujita and Y. Kawanishi, "Future pose prediction from 3d human skeleton sequence with surrounding situation," *Sensors*, vol. 23, no. 2, p. 876, 2023.
- [4] Y. Su, H. Hou, H. Lan, and C. Z.-H. Ma, "A high-fidelity mmwave radar dataset for privacy-sensitive human pose estimation," *Bioengineering*, vol. 12, no. 8, p. 891, 2025.
- [5] R. Liu, M. Li, Q. Liu, and A. L. Swindlehurst, "Snr/crb-constrained joint beamforming and reflection designs for ris-isac systems," *IEEE Transactions on Wireless Communications*, vol. 23, no. 7, pp. 7456–7470, 2023.
- [6] B. Li, X. Wang, and F. Fang, "Maximizing the value of service provisioning in multi-user isac systems through fairness guaranteed collaborative resource allocation," *IEEE Journal on Selected Areas in Communications*, vol. 42, no. 9, pp. 2243–2258, 2024.
- [7] Z. Ren, X. Song, Y. Fang, L. Qiu, and J. Xu, "Fundamental crb-rate tradeoff in multi-antenna multicast channel with isac," in

2022 IEEE Globecom Workshops (GC Wkshps), pp. 1261–1266, 2022.

- [8] Y. Wu, Z. Jiang, H. Ni, C. Mao, Z. Zhou, W. Wang, and J. Han, “mmhpe: Robust multiscale 3-d human pose estimation using a single mmwave radar,” *IEEE Internet of Things Journal*, vol. 12, no. 1, pp. 1032–1046, 2025.
- [9] H. Tang, W. Chen, Y. Yan, Y. Tang, Y. Yang, Y. Feng, X. Jiang, J. Lu, Y. Xu, and Q. Fang, “Gf-decnet: Geometry-aware feature decoupling network for millimeter-wave radar pose estimation,” *IEEE Internet of Things Journal*, 2025.
- [10] N. D. M. Quang, C. Liu, S. Li, H.-N. Vu, D. W. K. Ng, and W. Xiang, “Diffusion model-enhanced environment reconstruction in isac,” *IEEE Wireless Communications Letters*, vol. 15, pp. 1588–1592, 2026.
- [11] A. Jain, A. R. Zamir, S. Savarese, and A. Saxena, “Structural-rnn: Deep learning on spatio-temporal graphs,” in *Proceedings of the IEEE conference on computer vision and pattern recognition*, pp. 5308–5317, 2016.
- [12] Y. Ding, Y. Yang, J. Wang, Z. Yang, D. Niyato, Z. Han, and M. Shikh-Bahaei, “Energy efficient federated learning with hyperdimensional computing over wireless communication networks,” *arXiv preprint arXiv:2602.21949*, 2026.